Journal of Applied Physics

Donors and polaronic absorption in rutile TiO_2 single crystals

Cite as: J. Appl. Phys. **128**, 145701 (2020); https://doi.org/10.1063/5.0027434
Submitted: 28 August 2020 . Accepted: 21 September 2020 . Published Online: 08 October 2020

Philip Michael Weiser, Christian Zimmermann, Julie Bonkerud, Lasse Vines, and Eduard V. Monakhov

Journal of Applied Physics ARTICLE scitation.org/journal/jap

Donors and polaronic absorption in rutile TiO_2 single crystals

Cite as: J. Appl. Phys. **128**, 145701 (2020); doi: 10.1063/5.0027434
Submitted: 28 August 2020 · Accepted: 21 September 2020 ·
Published Online: 8 October 2020

Philip Michael Weiser,[a] Christian Zimmermann, Julie Bonkerud, Lasse Vines, and Eduard V. Monakhov

AFFILIATIONS

Department of Physics, Centre for Materials Science and Nanotechnology, University of Oslo, P.O. Box 1048, Blindern, Oslo N-0316, Norway

[a]**Author to whom correspondence should be addressed:** p.m.weiser@smn.uio.no

ABSTRACT

We have used a combination of optical absorption and electrical conductivity measurements to study the effect of the main donor on small polarons in rutile TiO_2 single crystals rendered *n*-type conductive by hydrogenation or doping with Nb. The electrical conductivity measured at 295 K for hydrogenated samples shows a clear correlation with the interstitial hydrogen (H_i) concentration, which is consistent with reports that H_i is the main shallow donor in rutile TiO_2. Conductive samples exhibit two distinct optical absorption bands in the IR spectral region, at $\omega_1 = 6500\ cm^{-1}$ (~0.8 eV) and $\omega_2 = 3100\ cm^{-1}$ (~0.4 eV), which are present in both hydrogen-rich and Nb-doped samples. The intensities of the absorption bands are proportional to the electrical conductivity, and they exhibit an Arrhenius-like temperature dependence for temperatures between 25–50 K and 50–100 K for H-doped and Nb-doped samples, respectively. The thermal activation energies (E_As) for the absorption bands depend strongly on the main donor: ω_2 exhibits $E_A(H)$ and $E_A(Nb)$ of ~4 and ~10 meV, respectively, whereas ω_1 shows $E_A(H)$ and $E_A(Nb)$ of ~1 and ~2 meV, respectively. The combination of temperature-dependent data for the optical absorption bands and interstitial deuterium (D_i)-small polaron vibrational lines support a model where the thermal activation is associated with the reconfiguration of small polarons involving Ti sites far away from the donor. The thermal activation of the optical absorption bands gives us insight into the dynamics of donor-dependent small polaron reconfiguration in rutile TiO_2.

I. INTRODUCTION

Titanium dioxide (TiO_2) is a wide bandgap semiconductor that received renewed interest in recent years for applications in photocatalysis, solar energy harvesting, and as an anode for Na ion batteries.[1–5] Its favorable chemical properties (earth abundant, nontoxic, and high stability), the commercial availability of bulk single crystals and nanocrystalline powders, and its early demonstration as an anode for photocatalytic water splitting have made TiO_2 the subject of intense research efforts for decades.[6] The most stable structural form, rutile, has a bandgap (E_g) of 3.0 eV,[7–9] making it transparent to visible (Vis) light. This intrinsic inability to utilize the Vis and infrared (IR) parts of the solar spectrum has severely hindered its further development as a photocatalyst. Research to improve the photocatalytic performance has focused on extending the optical absorption into the Vis spectral region.[10,11] The most promising approach involves high pressure hydrogenation of TiO_2 powders to create so-called black titania,[12] which extends the optical absorption into the IR spectral range. The success of TiO_2 as a photocatalyst has been attributed to the formation of various point defects during the hydrogenation process, but the exact nature [e.g., reduction of Ti^{4+} to Ti^{3+}, formation of oxygen vacancies (V_O), incorporation of hydrogen (H)] is still under debate.[13] It is therefore paramount to improve the fundamental understanding of point defects in rutile TiO_2 in order to shed light on the origin of the extended optical absorption.

As-grown rutile TiO_2 crystals are often semi-insulating and semi-transparent, but they can be doped *n*-type conductive by incorporation of different impurities: Li on interstitial sites,[14,15] P or Nb substitution on Ti sites,[16–18] and F substitution on O sites.[19] As the conductivity of a crystal increases, its color changes to gray (less conductive) to dark blue to silver/metallic (most conductive). Electron paramagnetic resonance (EPR) experiments and first-principles calculations[20–23] show that native V_O defects are shallow donors that can be present in as-grown crystals. Ionization energies of ~20 meV and 63 meV have been reported for Nb donors (Nb_{Ti})[24] and for the neutral charge state of V_O,[21] respectively.

Another common strategy to induce *n*-type conductivity is to anneal crystals in a reducing environment, such as hydrogen gas (H_2). On the basis of electron paramagnetic resonance (EPR) experiments by Chester,[25] the dominant donor in reduced samples was attributed to interstitial Ti (Ti_i) defects,[26] an assignment that has persisted for decades.[27,28] However, recent experiments by Brant *et al.*[29] show that the EPR signal in question actually originates from isolated interstitial H (H_i), casting doubt on the role of Ti_i. Furthermore, Ohlsen and Johnson[30] showed that crystals that were reduced in a clean vacuum remain insulating after being annealed at 1000 °C for up to 23 h, suggesting that the conductivity in "vacuum-reduced" crystals arises not from V_O or Ti_i, but rather from residual impurities, such as H.

Fundamental investigations into rutile TiO_2 are challenging due to the unique behavior of electrons in the material. In many other oxide semiconductors,[31] including anatase TiO_2,[32] free electrons are delocalized over many neighboring lattice sites and give rise to optical absorption originating from intraband transitions in the conduction band, i.e., Drude-like free-carrier absorption.[33] In contrast, conventional EPR experiments have shown that the wave function associated with a free electron in rutile TiO_2 is localized on a Ti^{4+} site regardless of the identity of the donor.[34] That is, it is energetically preferable for electrons to become self-trapped on Ti^{4+} sites and distort the surrounding lattice to form small polarons. The optical absorption due to small polarons is characterized by broad absorption that extends from the fundamental bandgap into the IR spectral region.[35–37] Unlike Drude-like free-carrier absorption, which increases as a function of the incident photon wavelength (λ) of $\lambda^{1.5-3.5}$ depending on the dominant scattering mechanism(s),[33] absorption due to small polarons achieves a maximum and is followed by a *decrease* in absorption strength with increasing λ. Similar absorption has been reported in other polaronic materials, including $LiNbO_3$,[38] $BaTiO_3$,[39,40] and WO_3.[41] Absorption by small polarons in rutile TiO_2 exhibits a maximum value in the near-IR (NIR) spectral region, most commonly at about 6600 cm^{-1} (0.82 eV). Extensive studies by Bogomolov and Mirlin[16,42] showed that the properties of the polaronic absorption in rutile TiO_2 are independent of the main donor and that the absorption amplitude is correlated with the electrical conductivity of the sample. Based on these observations, they proposed that the absorption arises from transitions of small polarons and is therefore a fingerprint for Ti^{3+} species. The exact nature of this absorption, e.g., polaron hopping vs excitation from the small polaron state to the conduction band minimum, is unknown. The small polaron model in rutile TiO_2 has been supported by other experimental techniques, including muon spin rotation spectroscopy (μSR),[43,44] and by first principles calculations.[22,23,45–48] Despite these insights, the nature of the charge transport (free carrier vs impurity band vs polaron related) remains unanswered. Recent first-principles calculations[23,45] suggest that small polarons and delocalized electrons can *coexist* in rutile TiO_2, with a small energy difference (<~0.1 eV) between the two states, and there is experimental evidence for this coexistence in reduced TiO_2 nanoparticles.[49] Experimental interpretations, however, are complicated by the fact that different characterization techniques might selectively measure the properties of either small polarons or delocalized electrons.

Hydrogen is a common impurity that is often incorporated unintentionally into semiconductor crystals during growth.[50] While the EPR studies conducted by Brant *et al.*[15] suggest that H_i is a shallow donor in rutile TiO_2, the behavior of H is generally unclear. A powerful method for understanding H-related point defects in semiconductors has been the characterization of impurity-related vibrations, so-called localized vibrational modes (LVMs).[51] The sensitivity of an impurity's LVM on the mass of the oscillating impurity and its local structure, which can include interactions with neighboring atoms, permits one to distinguish between different microscopic structures involving the same impurity atom. Infrared absorption measurements of intentionally hydrogenated rutile TiO_2 crystals reveal a number of H-related LVMs[35,52,53] that are all oriented perpendicular to the $\vec{c}$ axis of the crystal. A common LVM at 3278 cm^{-1} observed in both as-received and intentionally hydrogenated samples measured at room temperature (RT) has been attributed to H_i.[35,54] At cryogenic temperatures, this LVM splits into several peaks that show a complex temperature dependence. The same behavior is observed for its isotopic partner, interstitial deuterium (D_i). The temperature dependence of the LVMs was interpreted in terms of neutral and ionized states of a classical shallow donor, yielding an ionization energy of ~10 meV for H_i.[55] This interpretation is also supported by low temperature Hall effect[24] and photoconductivity measurements,[56] which yield similar ionization energies. However, Bekisli *et al.*[57] showed that the temperature dependence of the D_i LVMs could not be fit with a single thermal ionization energy and instead favored a model where the LVM splitting and their temperature dependences are explained by the different configurations of small polarons at Ti sites around the D_i (H_i) impurity. Thus, the role of H_i on the electrical conductivity of rutile TiO_2 is unclear from low temperature IR absorption experiments. In several metal oxide semiconductors, including ZnO,[58–60] In_2O_3,[61] SnO_2,[62,63] anatase TiO_2,[32] and, more recently, β–Ga_2O_3,[64] the role of different H-related point defects on the electrical conductivity was established by comparing the integrated absorbance of a defect's LVM, which is proportional to the defect's concentration, with the free carrier absorption strength. Such a comparison is strangely absent for the 3278 cm^{-1} H_i LVM and the polaronic absorption in rutile TiO_2.

A thorough understanding of the electrical and optical properties of the defects, specifically the donors, commonly found in rutile TiO_2 is crucial for the advancement of TiO_2-based applications. For example, Nitta *et al.*[65,66] examined the energy-resolved distribution of electron traps in TiO_2 powders by double-beam photoacoustic spectroscopy and observed a correlation between specific distributions of shallow electron traps and the photocatalytic activity. Another example is the recent electrical investigation of Nb-doped rutile TiO_2 single crystals by Kato *et al.*[67] They showed that an excess of Nb dopants might hinder, rather than promote, photocatalysis. The importance of H-related defects on the electrical conductivity of gas-hydrogenated rutile TiO_2 was questioned in a recent study by Mo *et al.*[68] Their data indicate that V_O, not H_i, is the main donor in gas-hydrogenated crystals and that H_i forms only in atom-hydrogenated (via chemical electrolysis) samples. Historically, first-principles calculations based on density-functional theory (DFT) have struggled to address the electrical behaviors and properties of point defects in polaronic materials due

to the effects of electron self-interaction errors.[22] While the use of hybrid functionals[22,23,45,69] has helped to address this issue, recent advances in first-principles calculations[70,71] show incredible potential for advancing a fundamental understanding of polarons and could benefit considerably from a modern set of experimental data.

In this work, we utilize a combination of optical and electrical measurements to study the optical absorption present in conductive *n*-type rutile TiO_2 single crystals, and its relation to the main donor in the material. We employ different doping strategies, e.g., by annealing TiO_2 in different reducing atmospheres (H_2, N_2, or a mixture of H_2 and N_2), or using Nb-doped crystals, to study the effects of different donors on its optical and electrical properties. The optical absorption at 295 K in the IR/Vis present in conductive *n*-type rutile TiO_2 displays a very similar spectral shape regardless of the main donor. In contrast to the report of Bogomolov and Mirlin,[42] we find that the optical absorption at low temperatures (<100 K) exhibits a *donor-dependent*, thermally activated behavior that is proposed to be related to the reconfiguration of small polarons.

II. EXPERIMENTAL METHODS

The rutile TiO_2 single crystals investigated in this work had a (001) surface orientation, double-sided polished surfaces, and dimensions of $10 \times 10 \times 0.5\ mm^3$. The as-received (as-rec.) single crystals were cut into four $5 \times 5\ mm^2$ pieces and cleaned in an ultrasonic bath with acetone, isopropanol, and de-ionized water for 5 min each. Highly resistive, transparent samples grown by the float zone method or the Verneuil method were purchased from MTI Corporation[72] and Shinkosha Co., Ltd.,[73] respectively. *N*-type conductive, Nb-doped samples grown by the Verneuil method were also purchased from Shinkosha Co., Ltd. with stated Nb concentrations, given in weight percent (wt. %), of 0.005, 0.010, and 0.050 wt. %. The donor concentration determined from C-V measurements on the 0.050 wt. % (corresponding to $[Nb] = 1.38 \times 10^{19}\ cm^{-3}$) Nb-doped sample has been shown[74] to be in excellent agreement with this stated value, which implies a negligible degree of compensation. The as-rec. semi-insulating crystals were annealed in one of the following three atmospheres to produce *n*-type conductive samples.[75]

(1) Forming gas (FG): annealed inside a tube furnace while directly exposed to flowing forming gas (with $[H_2]/[N_2] \sim 1/9$) at 600 °C for 5–90 min.
(2) Nitrogen gas (N_2): annealed inside a tube furnace while directly exposed to flowing nitrogen gas at temperatures between 1100 and 1200 °C for 5–90 min.
(3) Hydrogen gas (H_2): annealed inside a sealed quartz ampoule filled with 0.5 bar of hydrogen gas at room temperature (RT). The ampoule was placed inside a tube furnace at temperatures between 400 and 450 °C for 30–90 min.

In addition, one as-rec. sample was annealed at 400 °C for 60 min in an ampoule filled with 0.5 bar of deuterium gas (D_2) at RT. Samples annealed in flowing gas were removed from the furnace upon completion of the annealing and cooled in air, whereas those annealed in ampoules were cooled outside the furnace while still inside the ampoule. All of the annealed samples were washed in acetone, isopropanol, and de-ionized water following cool down. None of the Nb-doped crystals were subjected to gas annealing.

The electrical and optical properties of each sample were investigated at RT to examine the relationship between the sample conductivity and the optical absorption. The electrical conductivity was calculated from resistivity measurements in the Van der Pauw configuration[76–78] using a four-point probe setup consisting of a Keithley 7001 switch system, a Keithley 2182A nano-volt-meter, and a Keithley 6221 current source. Eutectic InGa was scratched into the corners of each sample to create Ohmic contacts. Optical transmittance spectra were measured using a Bruker IFS 125HR Fourier Transform (FT) spectrometer [spectral resolution (res) = $4\ cm^{-1}$] and a Shimadzu SolidSpec-3700DUV UV-Vis-NIR spectrophotometer (res = 1 nm). The FT spectrometer provided access to the mid-IR (MIR) spectral range ($600–4000\ cm^{-1}$) using a globar light source, a KBr beam splitter, and a MCT detector; and to the NIR range ($4000–9600\ cm^{-1}$) using a quartz light source, a CaF_2 beam splitter, and an InSb detector. Transmittance spectra acquired on the UV-Vis spectrophotometer utilized a tungsten lamp and three different detectors (PbS, InGaAs, and a photomultiplier tube) to measure from the NIR to the UV spectral range ($6000–30\,000\ cm^{-1}$). Unpolarized light was directed at normal incidence (±3°) to the (001) surface of the sample such that the electric field was perpendicular to the *c*-axis ($\vec{E} \perp \vec{c}$). The empty sample holder served as the background/reference for all measurements. The full optical transmittance spectrum for each sample was obtained by combining the spectral data in their overlapping regions. It should be noted that the thickness of the 0.050 wt. % Nb-doped sample was reduced to 300 μm by lapping and polishing the surface in SiC and diamond paste, respectively, in order to avoid total absorption.

To study the effect of temperature on the optical properties, samples were measured in the temperature range between 5 and 295 K. These measurements were restricted to the MIR and NIR setups on the FT spectrometer. The samples were cooled in a Janis PTSHI-950-5 closed cycle, continuous flow cryostat equipped with ZnSe cold windows. The samples were surrounded by He-exchange gas and their temperatures were varied to within ±0.1 K using a LakeShore Model 335 temperature controller. Transmittance data (T) were converted to absorption coefficient data (α) using the standard analytical solution[79] to

$$T = \frac{(1-R)^2 \exp(-\alpha d)}{1 - R^2 \exp(-2\alpha d)};\ R = \frac{|\tilde{n}-1|^2}{|\tilde{n}+1|^2}. \quad (1)$$

Here, d is the thickness of the sample and R is the reflectivity as determined by the complex refractive index $\tilde{n}$. The spectral range of our measurements is limited at low incident photon energies by multiphonon absorption and at high incident photon energies by fundamental-band-to-band absorption. For the spectral region between 1800 and $22\,500\ cm^{-1}$, we use $\tilde{n} = 2.44$ ($\vec{E} \perp \vec{c}$, rutile)[80] to calculate α in Eq. (1). For analysis of the changes to the optical absorption for different conductivities or different temperatures, the α spectrum of a semi-insulating as-rec. sample was subtracted from the α spectrum of every conductive sample to produce a $\Delta\alpha$

spectrum, which accounts for the slight variation in $\tilde{n}$ across the measured spectral region.

The LVMs of H_i and D_i were measured using the Bruker FT spectrometer equipped with a globar light source, a KBr beam splitter, and an InSb detector. Measurements at RT used a spectral resolution of 1.0 cm^{-1}, whereas low temperature (LT) measurements ($T < 60$ K) used a spectral resolution of 0.1 cm^{-1}. The LT measurements were performed with the incident light directed parallel to the (001) surface of the crystal (i.e., with $d \sim 5$ mm) to suppress interference fringes arising from multiple surface reflections. The H_i concentration ($[H_i]$) was determined by correcting α spectra [also calculated using Eq. (1)] with a spline-interpolated baseline using points placed along the broad absorption between 3100 and 3500 cm^{-1}. The RT LVMs were fit with Lorentzian line shapes, whereas those at LT were fit with Voigt line shapes.[57] In both cases, the integrated absorption coefficient (int. α) was determined analytically from the line shapes. The $[H_i]$ was calculated[51] from the int. α of the 3278 cm^{-1} LVM measured at RT using a calibration factor of 1.73×10^{16} cm^{-1} determined from the data of Johnson *et al.*[81]

III. RESULTS

The annealing treatments in FG, H_2, or N_2 produced samples ranging from light gray to light blue in color, depending on the temperature and the duration of the anneal. Similar color differences were observed for the as-rec. Nb-doped samples.

Figure 1(a) shows α spectra measured at RT for selected rutile TiO_2 samples with different treatments and different conductivities. The majority of the samples show absorption across the sub-bandgap region, which is dominated by a broad, asymmetric absorption band (denoted as ω_1) whose maximum occurs between 6000 and 6500 cm^{-1} in the NIR spectral region. The high-energy side of ω_1 shows a gradual decrease in strength; except for a few N_2-annealed samples, no additional features are present in this region. Two features are noted on the low energy side of ω_1: a weak, broad shoulder that produces a local maximum near 3100 cm^{-1} (0.38 eV), denoted as ω_2, and a narrow vibrational line at 3278 cm^{-1} due to isolated H_i. In one FG-annealed sample (not shown), ω_1's maximum is blue shifted to 8750 cm^{-1}, which is similar to what has been reported by Cronemeyer.[7–9] The shape and strength of ω_1 in the majority of the samples, however, are consistent with reports from various authors.[35–37] Interestingly, the ω_2 peak was not reported in early experiments and was only identified recently by Khomenko *et al.* in strongly absorbing H-containing samples.[37] Figure 1(b) shows the baseline-corrected α spectra in the OH spectral region for the samples whose α spectra are shown in panel (a). The H_i LVM dominates in the FG- and H_2-annealed samples, whereas it is much weaker in the N_2-annealed samples. In the Nb-doped samples, the H_i LVM is detected in only one sample (0.010 wt. %), but it is considerably weaker than the H_i LVM observed in the as-received or N_2-annealed samples. The H_i LVM was below the detection limit of $\sim 10^{15}$ cm^{-3} for measurements at 5 K in the 0.005 wt. % and 0.050 wt. % Nb-doped samples. Several FG- and H_2-annealed samples also show a LVM at 3345 cm^{-1} that has been assigned to H_i near a Mg impurity substituting on a Ti site (Mg_{Ti}-H_i).[52] The amplitude of α for the Mg_{Ti}-H_i LVM is typically

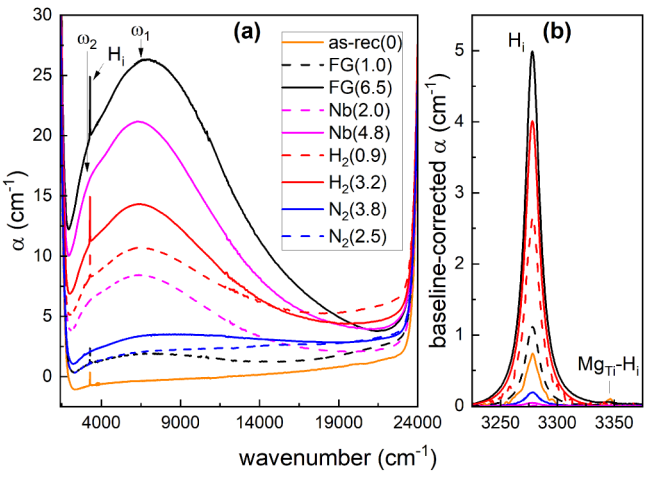

FIG. 1. (a) α spectra at 295 K for different FG-annealed, H_2-annealed, N_2-annealed, and Nb-doped rutile TiO_2 samples (distinguished by color). The electrical conductivity (in Ω^{-1} m^{-1}) of each sample is indicated in parenthesis in the legend. Absorption bands at 6500 and 3100 cm^{-1} are labeled ω_1 and ω_2, respectively. The 3278-cm^{-1} LVM due to isolated H_i is also indicated. Noise artifacts due to detector and grating changes between 10 900 and 11 800 cm^{-1} have been removed for visual clarity. (b) α spectra at 295 K of H-related LVMs for the samples shown in panel (a). The styles of the spectra match between the two panels. The spectral region between 3100 and 3500 cm^{-1} was corrected using a spline baseline for visual clarity. A weak LVM at 3345 cm^{-1} assigned to a Mg_{Ti}-H_i complex is noted in addition to the 3278-cm^{-1} H_i LVM.

1%–10% of the amplitude of the 3278-cm^{-1} H_i LVM, which suggests that isolated H_i is the dominant H-related defect in these samples.

The strength of the 3278 cm^{-1} H_i LVM [Fig. 1(b)] increases considerably in the FG- and H_2-annealed samples compared to the strength in the as-rec. crystals. Figure 2(a) shows a log-log plot of the $[H_i]$ vs the electrical conductivity for FG-, H_2-, and N_2-annealed samples. There is a strong linear correlation between the $[H_i]$ and the electrical conductivity in the FG- and H_2-annealed samples, which is consistent with previous reports that H_i is the main donor in hydrogenated rutile TiO_2.[55] The linear fit determined from a least squares analysis of the data shown in Fig. 2 yields

$$[H_i][cm^{-3}] = (4.2 \pm 0.4) \times 10^{19} \Omega\, cm^{-2} \times \sigma, \quad (2)$$

where σ is the electrical conductivity (given in Ω^{-1} cm^{-1}). The uncertainties in the fit parameters are determined from the scatter of the data in the fit. The choice of the specific constraint on the y-intercept (e.g., equal to 0, equal to the $[H_i]$ in the as-rec. samples, or free parameter) has a negligible impact on the slope in Eq. (2) within the error of the fit. The conductivities of the Nb-doped samples show no dependence on the $[H_i]$, but do show a linear dependence on the nominal $[Nb_{Ti}]$, as expected. A linear fit to these data yields

$$[Nb_{Ti}][cm^{-3}] = (5.4 \pm 0.1) \times 10^{19}\, \Omega\, cm^{-2} \times \sigma, \quad (3)$$

where σ is again given in Ω^{-1} cm^{-1}. Assuming negligible

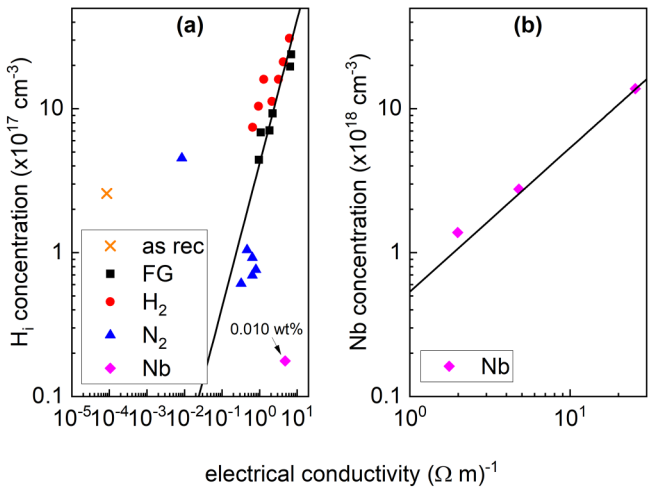

FIG. 2. Plots of the $[H_i]$ (a) and the nominal $[Nb_{Ti}]$ (b) vs the electrical conductivity for n-type conductive rutile TiO_2 samples. The solid black line in each panel is a linear fit to the data (filled points) with the y-intercept constrained to zero. The fit shown in panel (a) is to the data for the FG- and H_2-annealed samples, whereas the fit shown in panel (b) is for the Nb-doped samples. The $[H_i]$ in the 0.005 and 0.050 wt. % Nb-doped samples is below the detection limit (at 5 K) of ~10^{15} cm^{-3} and are therefore not shown in panel (a).

compensation, the electron mobility (μ) at RT for H-doped and Nb-doped rutile TiO_2 can be estimated using the relationship

$$N = \frac{1}{e\mu}\sigma, \tag{4}$$

where N is the donor concentration (in cm^{-3}) and e is the elementary charge. Using the slopes of the fits shown in Eqs. (2) and (3), we determine μ_H (295 K) = 0.15 ± 0.01 cm^2 V^{-1} s^{-1} and μ_{Nb} (295 K) = 0.12 ± 0.01 cm^2 V^{-1} s^{-1}, which are consistent with values of 0.1–1 cm^2 V^{-1} s^{-1} reported in the literature for both H- and Nb-doped samples.[36,42,82]

The amplitudes of ω_1 and ω_2 increase as the samples become darker in color (Fig. 1), but both the strength of ω_1 and its large width complicates the analysis of ω_2. In order to separate ω_2's contribution from that of ω_1's, each α spectrum was fit with two Gaussian line shapes: a broad band centered near ω_1 and a weaker band at ω_2. An example of a typical fit to the data is shown in Fig. 3. All fits were performed using a least squares approach as implemented in the Python library "scipy" and were restricted to the region between 2000 and 6700 cm^{-1}. There is satisfactory agreement between the fits and the data on the low energy side of ω_1. We have chosen to work with the integrated α (the analytical area of the Gaussian line shape) of ω_2 because the shape of the band is simple. The shape of the ω_1 absorption band, on the other hand, is complicated, and a Gaussian line shape cannot properly capture the absorption at increasing incident photon energies. Other line shapes, e.g., absorption from a deep-level defect,[83] have been tested to improve the fit for ω_1, but do not offer a considerable

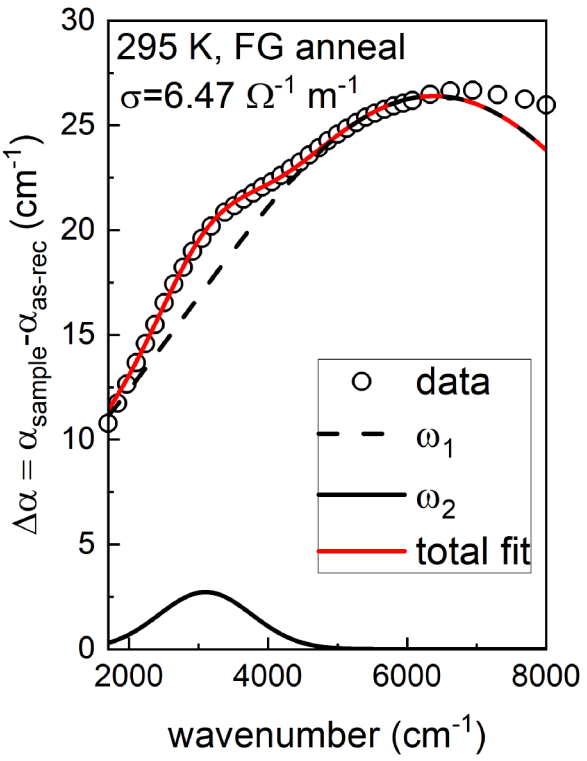

FIG. 3. Δα spectrum (at RT) for a FG-annealed rutile TiO_2 sample (open circles). A broad Gaussian band centered near ω_1 (dashed black curve) serves as the baseline for the weaker Gaussian band at ω_2 (solid black curve). The sum of ω_1 and ω_2 yields the total fit (solid red curve) to the IR spectral region. The fit was determined using a least squares approach within the range of 2000 and 6700 cm^{-1}.

improvement to justify their use, and produce similar ω_2 contributions. Therefore, we use the amplitude of ω_1, rather than its area, for our analysis.

Figure 4 shows the amplitude of ω_1 and the integrated $\Delta\alpha$ of ω_2, as determined from its Gaussian fit, vs σ for all of the samples. Both sets of data show a clear linear correlation with σ, which can be expressed by

$$\frac{\Delta\alpha_{max}(\omega_1)\ [\mathrm{cm}^{-1}]}{\sigma[\Omega^{-1}\ \mathrm{cm}^{-1}]} = (470 \pm 30)\ \Omega \tag{5}$$

and

$$\frac{\int \Delta\alpha(\omega_2)d\omega\ [\mathrm{cm}^{-2}]}{\sigma[\Omega^{-1}\ \mathrm{cm}^{-1}]} = (10 \pm 2) \times 10^4\ \Omega\,\mathrm{cm}^{-1}. \tag{6}$$

The linear correlation between $\Delta\alpha_{max}(\omega_1)$ and σ was previously established by Bogomolov and Mirlin.[42] They determined a slope of (530 ± 50) Ω, which is in good agreement with the value shown in Eq. (5). However, the linear correlation between the int. $\Delta\alpha$ of ω_2 and σ has not been reported before. The linear fits for ω_2

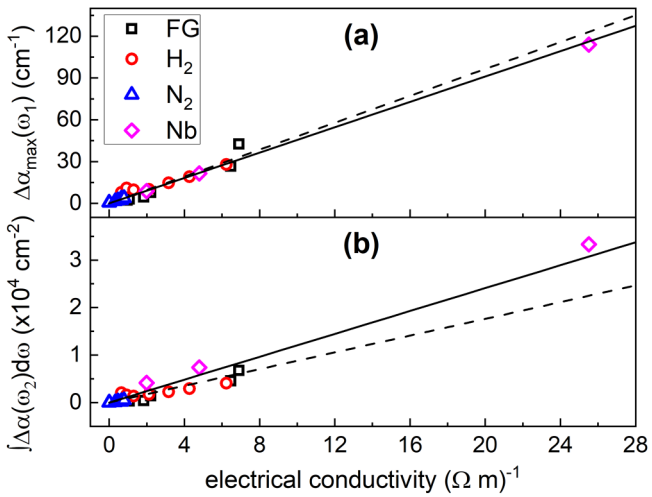

FIG. 4. Maximum amplitude of ω_1 (a) and int. abs. coef. of ω_2 (b) vs the electrical conductivity at RT for gas-annealed and Nb-doped rutile TiO_2. The points correspond to data for the differently doped samples. The solid line in each panel is the linear fit including all of the data, whereas the dashed line excludes the 0.050 wt. % Nb-doped sample ($\sigma = 25.5\ \Omega^{-1}\ m^{-1}$).

shown in Fig. 4 have slopes in the range of $(8.8–12) \times 10^4\ \Omega\ cm^{-1}$. (The corresponding slope using ω_2's amplitude is in the range of 45–63 Ω, which is approximately one order of magnitude less than the slope for ω_1.)

The temperature dependence of α at cryogenic temperatures in several TiO_2 samples was investigated for the gas-annealed samples and the Nb-doped crystals. Figure 5 shows the dependence of $\Delta\alpha$ for a FG-annealed sample for temperatures between 20 and 55 K (panel a) and between 55 and 100 K (panel b). No significant changes to $\Delta\alpha$ are observed for temperatures between 5 and 20 K. As the temperature increases from 20 to 50 K, the amplitudes of ω_1 and ω_2 increase considerably. In fact, at 50 K, ω_2 has increased such that it is clearly distinguishable from the dominant ω_1 band. As the temperature continues to increase above 50 K, ω_1 remains relatively unchanged whereas ω_2 *decreases in strength*. This behavior is also observed in the other samples where H_i is the dominant donor.

Figure 6 shows the temperature dependence of $\Delta\alpha$ for the 0.010% wt. % Nb-doped sample, which is representative of the behavior observed in the 0.005 wt. % and 0.050 wt. % Nb-doped samples. The amplitudes of ω_1 and ω_2 increase in strength as the temperature increases, but in contrast to the H-doped sample shown in Fig. 5, the temperature range where this increase occurs is between 50 and up to 95 K. For temperatures above 100 K, both ω_1 and ω_2 decrease in strength. The changes in the $\Delta\alpha$ spectra reported for both H- and Nb-doped samples are reproducible regardless of the number of times the samples were thermally cycled between LT and RT. A similar trend for the evolution of ω_2 was also observed for the conductive N_2-annealed samples, but the low conductivity (and hence weak absorption) made it difficult to study the temperature dependence of $\Delta\alpha$ in these samples.

To analyze the changes to ω_1 and ω_2 with respect to measurement temperature, each spectrum was fit using the method shown in Fig. 3, i.e., ω_1 and ω_2 were fit using Gaussian line shapes. Figure 7 shows Arrhenius plots for the normalized amplitudes of ω_1 (panel a) and the normalized areas of ω_2 (panel b) for the H-doped and Nb-doped samples shown in Figs. 5 and 6, respectively. Below their respective onset temperatures (~25 K for H and ~50 K for Nb), both ω_1 and ω_2 are independent of temperature. For both the H- and the Nb-doped samples, the intensities of ω_1 and ω_2 increase linearly (on a logarithmic scale) with decreasing 1/T, which suggests that their individual thermal activations can be described by a single activation energy (E_A).

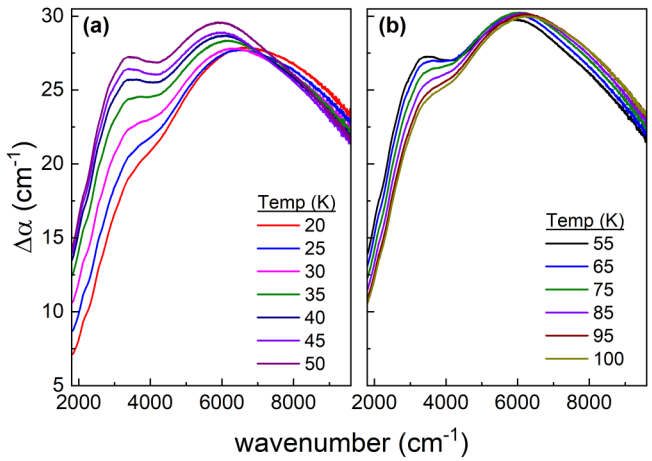

FIG. 5. $\Delta\alpha$ spectra for a H-doped TiO_2 sample (FG-annealed, $\sigma = 6.5\ \Omega^{-1}\ m^{-1}$) between (a) 20 and 50 K and (b) 55 and 100 K. The spectral region between 3239 and 3391 cm^{-1} (H_i LVM) has been removed for visual clarity.

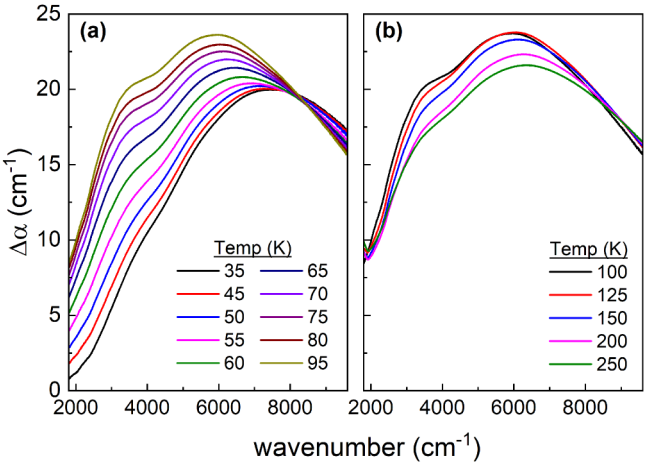

FIG. 6. $\Delta\alpha$ spectra for the 0.010 wt. % Nb-doped TiO_2 sample ($\sigma = 4.8\ \Omega^{-1}\ m^{-1}$) between (a) 35 and 95 K and (b) 100 and 250 K. The spectral region between 3239 and 3391 cm^{-1} (H_i LVM) has been removed for visual clarity.

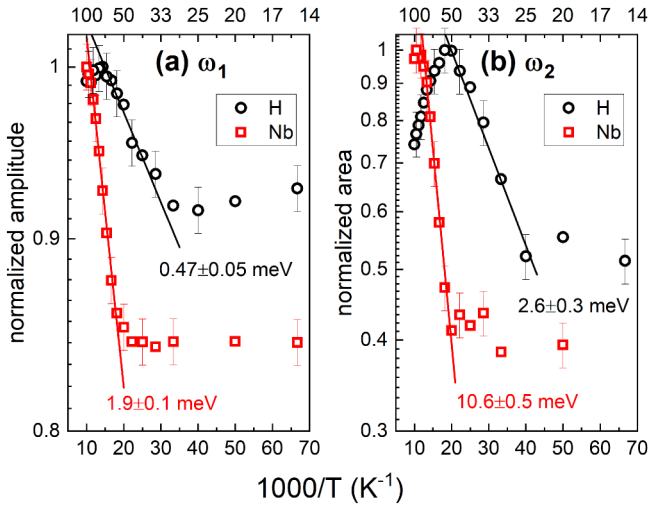

FIG. 7. Arrhenius plots of (a) the normalized amplitude of ω_1 and (b) the normalized area of ω_2 for the H-doped (open black circles) and Nb-doped (open red squares) rutile TiO_2 samples shown in Figs. 5 and 6, respectively. The corresponding measurement temperature is indicated on the upper horizontal axis. The uncertainties stated for the linear fits are calculated from the scatter in the data. Error bars are shown on only every other data point for clarity.

Ranges for the E_As for ω_1 and ω_2 for H_i and Nb_{Ti} donors are shown in Table I and were determined using five different H-doped samples and three different Nb-doped samples. (An activation energy of $E_A(\omega_2) = 3 \pm 1$ meV could be determined for only the most conductive N_2-annealed sample.) The main donor has a pronounced effect on the E_As; for both ω_1 and ω_2, samples containing Nb_{Ti} donors exhibit higher E_As than the samples containing H_i donors. Furthermore, there is a significant difference between the activation energies for ω_1 and ω_2 for the same main donor.

The absorbance spectra for the D_2-annealed sample are presented in Fig. 8, where panels (a) and (b) show the temperature dependence of the D_i LVMs and $\Delta\alpha$, respectively. The D_i LVMs at 2445.0 and 2447.8 cm^{-1} are denoted as ω_a and ω_c, respectively. As T increases from 5 to 20 K, the strength of ω_a decreases and the strength of ω_c increases, whereas the reverse trend (increase in ω_a and decrease in ω_c) is seen for T at and above 20 K. The temperature dependence of the D_i LVMs observed in our sample is similar to the one reported by Bekisli *et al.*[57] The temperature dependence of α in the D_2-annealed sample [Fig. 8(b)] is similar to the one which is observed in the H_2-annealed samples. Below 20 K, the spectrum is largely unchanged, whereas the intensities of both ω_1 and ω_2 increase as T increases up to 55 K. Figure 8(c) shows the normalized values for the ratio of the area of ω_c to the area of ω_a, the area of ω_2, and the amplitude of ω_1 between 5 and 55 K.

Changes in the intensities of the D_i LVMs are seen for $T < 25$ K, but no change in the strength of ω_1 or ω_2 is observed. At $T > 25$ K, we observe an anticorrelation between the ratio of the areas of the D_i LVMs and the amplitude of ω_1 and the area of ω_2, which suggests that the mechanism responsible for the changes in the D_i LVMs is also connected to the activation of ω_1 and ω_2.

TABLE I. Experimentally determined E_A ranges for the ω_1 and ω_2 absorption bands in rutile TiO_2 for H_i and Nb_{Ti} donors.

Donor	$E_A(\omega_1)$ (meV)	$E_A(\omega_2)$ (meV)
H_i	0.5–1.0	2.5–5.0
Nb_{Ti}	1.4–2.2	8.6–10.6

IV. DISCUSSION

A recent study by Mo *et al.*[68] proposed that gas hydrogenation of rutile TiO_2 creates mainly hydrogen substituting at an oxygen site (H_O), rather than H_i, and produces IR-transparent crystals. However, the α spectra in Fig. 1 show that gas hydrogenation consistently produces H_i and gives rise to substantial optical absorption at energies below the fundamental bandgap, especially in the IR spectral region, that is proportional to the electrical conductivity of the samples. The linear relation between the $[H_i]$ and σ shown in Fig. 2(a) is consistent with reports in the literature that annealing rutile TiO_2 single crystals in an H_2-containing atmosphere increases the electrical conductivity. Our results suggest that the electrical conductivity increases as a result of the increasing concentration of H_i shallow donors, which is consistent with recent hybrid-DFT calculations by Bjørheim *et al.*[69] The linear relationship between $[H_i]$ and σ also holds for the N_2-annealed samples, which have considerably higher conductivities but about an order of magnitude *less* H_i than the as-received samples. This apparent contradiction can be explained if the heat treatments lead to both a significant lowering of the concentration(s) of compensating acceptor(s) and a decrease in $[H_i]$. Thus, H_i is likely to be the main donor in N_2-annealed samples even though these samples exhibit a lower $[H_i]$ than as-received samples. However, first-principles calculations by Han *et al.*[84] predict H_O, rather than H_i, is the main H-related donor in rutile TiO_2, which is in contrast to the calculations by Bjørheim *et al.*[69] The LVM due to H_O occurs typically at lower wavenumbers where the crystal is opaque to IR light, which prevents its observation in our measurements. Therefore, our data do not allow us to completely exclude the possibility that the electrical conductivity increase is due, at least partially, to the formation of H_O.

We now focus on the results related to the optical absorption present in *n*-type conductive rutile TiO_2. Several authors have claimed that the absorption in rutile TiO_2 crystals induced by doping with H or Nb is due to Drude-like free-carrier absorption.[55,67] Although the dependence of α in the Vis and NIR spectral regions resembles the absorption of Drude-like free carriers, all of our conductive rutile TiO_2 crystals exhibit a *decrease* in α for photon energies below the maximum amplitude of ω_1, which is incompatible with the Drude theory. We find that the α spectra of conductive rutile TiO_2 samples show at least two distinct features (ω_1 and ω_2) in the sub-bandgap region whose intensities are linearly correlated with the electrical conductivity. Our data for ω_1 are in agreement with the results of Bogomolov and Mirlin,[42] who proposed that this feature originates from transitions associated with small polarons. However, the independence of the presence of ω_2 on the main donor and its linear correlation with the

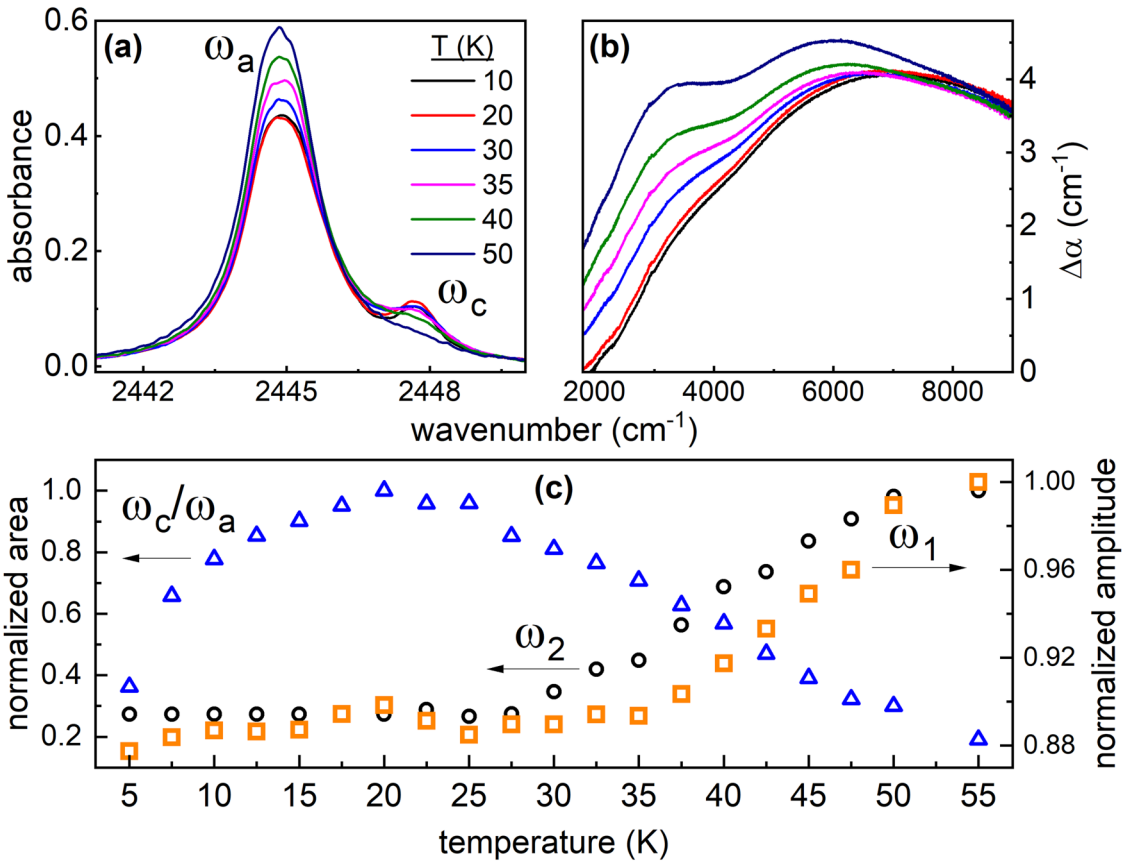

FIG. 8. (a) D_i LVM absorbance spectra and (b) $\Delta\alpha$ spectra of the D_2-annealed rutile TiO_2 crystal at temperatures between 10 and 50 K. The legend shown in panel (a) also applies to the spectra shown in panel (b). The D_i LVMs were removed from the α spectra shown in (b) for visual clarity. (c) The normalized areas of ω_c/ω_a (blue triangles) and ω_2 (black circles), and the normalized amplitude of ω_1 (orange squares) for temperatures between 5 and 55 K.

electrical conductivity has not been demonstrated. The similar behaviors observed for ω_1 and ω_2 lead us to propose that both of these absorption bands originate from optical transitions of small polarons. Recent first-principles calculations by Atambo *et al.*[46] predict absorption features at 0.33 and 0.60 eV in H-doped and at 0.35 and 0.93 eV in Nb-doped rutile TiO_2, which they assign to transitions from donor-bound electron polarons to the conduction band minimum. We observe that the maxima of ω_2 and ω_1 occur (at LT) near 3300 cm^{-1} (0.41 eV) and 6600 cm^{-1} (0.82 eV) in H-doped and near 3700 cm^{-1} (0.46 eV) and 7500 cm^{-1} (0.93 eV) in Nb-doped samples. Thus, there is good agreement for both dopants between the positions of our measured absorption bands and their calculated transition energies. However, the different E_As for ω_1 vs ω_2 determined from the temperature dependence of α between 5 and 100 K imply that these transitions are due to two different processes, e.g., excitation to the conduction band, transitions from bound polarons, polaron hopping, but a definitive assignment is not possible here.

Our LT optical measurements of H-doped and Nb-doped rutile TiO_2 offer new insights into the properties of small polarons and their behavior in this material. Bekisli *et al.*[57] explained the temperature dependence of the D_i LVMs at LT in terms of a three-level system where each level represents the localization of an electron on a different Ti site neighboring D_i. We consider a three-level system similar to that of Bekisli's: two of the levels (E_1 and E_3) give rise to the same D_i LVM (ω_a) and the remaining level (E_2) gives rise to a different LVM (ω_c). At 5 K, most of the electrons are localized on Ti sites neighboring D_i and occupy mainly state E_1. As T increases to 20 K, electrons can migrate and localize on other neighboring Ti sites to occupy state E_2 and shift the intensity of the D_i LVMs from ω_a to ω_c. As T increases even more, from 20 to 55 K, reconfiguration results in an increased population of electrons at Ti sites further away from D_i, resulting in an intensity shift from ω_c back to ω_a. They noted that E_3 does not correspond to one specific Ti site, but rather to many Ti sites located further away from D_i than the Ti sites corresponding to configurations E_1 and E_2. Bekisli determined thermal activation energies between E_1 and E_2 and between E_2 and E_3 of 0.5 and 11 meV, respectively, for D_i and similar values for H_i. We obtain similar activation energies for our temperature dependent D_i data using their fitting procedure (not shown).

The model proposed by Bekisli provides one possible explanation for the thermal activation of ω_1 and ω_2: the reconfiguration of small polarons to Ti sites located further away from the donor. This interpretation is driven primarily by the anticorrelation between the ratio of the D_i LVMs (ω_c/ω_a) and the absorption bands (ω_1 and ω_2), which is not possible for the majority of other donors, e.g., Li, P, and F, because they do not give rise to measurable vibrational lines. Despite the fact that the small polarons are localized far away from the donor, the different E_A's for H-doped and Nb-doped samples show that the main donor has a significant effect on the reconfiguration process. Low temperature EPR measurements[34] show consistently that free electrons are localized on Ti sites at 5 K, i.e., the donors are already ionized at 5 K. In the context of this model, the E_As determined from our temperature-dependent absorption measurements are not indicative of polaron-donor binding energies, but rather of the dynamics of small-polaron reconfiguration among Ti sites.

So far, we have not attempted to connect the polaronic absorption bands (ω_1 and ω_2) to the three-level system used to model the D_i LVMs. At temperatures between 10 and 25 K, the intensities of the D_i LVMs change considerably, whereas there are negligible changes to ω_1 and ω_2. Thus, it is unlikely that the polaronic absorption bands originate from the E_1 or E_2 states. Both ω_a (D_i LVM corresponding to the E_3 level) and the polaronic absorption bands are thermally activated in the same temperature range (above 25 K), which suggests, on the one hand, that ω_1 and ω_2 could originate from the E_3 state. On the other hand, it is possible that the polaronic absorption originates from another channel (e.g., free polarons), and the coinciding thermally activated behaviors is the result of polaron redistribution from the E_1 and E_2 states to both E_3 and the alternative channel(s) from which ω_1 and ω_2 originate. Our data do not allow us to decide which model is more likely. Furthermore, the amplitudes of ω_1 and ω_2 are already quite strong (~30%–40% and 80%–90% of their maximum intensities, respectively) below their respective onset temperatures: ~25 K for H_i donors and ~50 K for Nb_{Ti} donors. Our data alone cannot explain this surprising behavior, and further experimental and theoretical investigations are needed to clarify its origin.

Previous investigations of the optical absorption[37,42] claim that the intensity of ω_1 continues to *increase* from cryogenic temperatures to 295 K. It is evident from Figs. 5 and 6 that both ω_1 and ω_2 experience a thermal deactivation process by which their intensities *decrease* as T increases to 295 K. For H-doped samples, the thermal deactivation of ω_2 starts immediately after it reaches its maximum value ($T \sim 55$ K). The behavior of ω_1 is less clear: in some samples, the amplitude remains constant up to 100 K and then begins to decrease, whereas in other samples the amplitude continues to increase up to 100 K. For Nb-doped samples, ω_1 and ω_2 appear to deactivate at higher temperatures: ~100 K for ω_2 and ~125 K for ω_1. Additional investigations are called for to clarify the origin of the deactivation mechanisms.

V. CONCLUSIONS

The influence of the main donor on the optical and electrical properties of rutile TiO_2 single crystals was studied in samples rendered *n*-type conductive and doped with either Nb or H. The Nb-doped samples contain negligible amounts of H_i compared to the nominal Nb concentration, which establishes Nb_{Ti} as the main donor. In the gas-annealed samples, we show that H_i is the main H-related defect and potentially the main donor. The optical absorption spectra of conductive rutile TiO_2 crystals exhibit two absorption features in the IR spectral region (ω_1 and ω_2) whose presences are independent of the main donor and whose intensities are linearly correlated with the electrical conductivity and, therefore, are proposed to originate from small polarons. The combination of temperature-dependent data for optical absorption and defect LVMs provides a powerful picture of the behavior of small polarons in rutile TiO_2. Our data support a model where ω_1 and ω_2 are thermally activated by the reconfiguration of small polarons to Ti sites further away from the donor, a process which is itself affected by the main donor (H_i or Nb_{Ti}). We determine E_A ranges for ω_2 of 2.5–5.0 meV and 8.6–10.6 meV for H_i and Nb_{Ti}, respectively, and for ω_1 of 0.5–1.0 meV and 1.4–2.2 meV for H_i and Nb_{Ti}, respectively. The thermal activation of the optical absorption bands gives insight into the dynamics of polaron reconfiguration near the donors, which allows for a systematic study of different donors that do not give rise to observable LVMs, e.g., V_O, Li, and F. Knowledge of the reconfiguration energies for these other donors would provide a solid experimental foundation to compare with the results of first-principles calculations. Such information is crucial to fully understand and control the behavior of small polarons in rutile TiO_2 and other polaronic materials.

ACKNOWLEDGMENTS

We gratefully acknowledge K. Irmscher and M. Pietsch (IKZ Berlin) for their support of low temperature UV Vis optical measurements, O. B. Karlsen (University of Oslo) for his assistance with preparing the ampoules, and H. N. Riise and M. Nyborg for their assistance with the Hall effect measurements and interpretation. We are grateful to R. Karsthof for proofreading the manuscript and for discussions about small polarons. Funding for this work was provided by the Norwegian Research Council through the Research Center for Sustainable Solar Cell Technology (FME SuSolTech, No. 257639), the Norwegian Micro- and Nano-Fabrication Facility (NorFab, No. 245963), and the Norwegian PhD Network on Nanotechnology for Microsystems (No. 221860/F60). We also acknowledge the Faculty of Mathematics and Natural Sciences at the University of Oslo for their financial support via the strategic research initiative, FOXHOUND.

DATA AVAILABILITY

The data that support the findings of this study are available from the corresponding author upon reasonable request.

REFERENCES

[1] A. Fujishima, X. Zhang, and D. Tryk, Surf. Sci. Rep. **63**, 515 (2008).
[2] Y. Li, J. K. Cooper, W. Liu, C. M. Sutter-Fella, M. Amani, J. W. Beeman, A. Javey, J. W. Ager, Y. Liu, F. M. Toma, and I. D. Sharp, Nat. Commun. **7**, 12446 (2016).
[3] A. Naldoni, M. Altomare, G. Zoppellaro, N. Liu, S. Kment, R. Zboril, and P. Schmuki, ACS Catal. **9**, 345 (2019).
[4] A. Miyoshi, S. Nishioka, and K. Maeda, Chem. A Eur. J. **24**, 18204 (2018).

[5]H. Usui, S. Yoshioka, K. Wasada, M. Shimizu, and H. Sakaguchi, ACS Appl. Mater. Interfaces **7**, 6567 (2015).
[6]F. A. Grant, Rev. Mod. Phys. **31**, 646 (1959).
[7]D. C. Cronemeyer and M. A. Gilleo, Phys. Rev. **82**, 975 (1951).
[8]D. C. Cronemeyer, Phys. Rev. **87**, 876 (1952).
[9]D. C. Cronemeyer, Phys. Rev. **113**, 1222 (1959).
[10]J. Schneider, M. Matsuoka, M. Takeuchi, J. Zhang, Y. Horiuchi, M. Anpo, and D. W. Bahnemann, Chem. Rev. **114**, 9919 (2014).
[11]H. Wang and J. P. Lewis, J. Phys. Condens. Matter **18**, 2 (2005).
[12]Z. Wang, C. Yang, T. Lin, H. Yin, P. Chen, D. Wan, F. Xu, F. Huang, J. Lin, X. Xie, and M. Jiang, Adv. Funct. Mater. **23**, 5444 (2013).
[13]A. Chatzitakis and S. Sartori, ChemPhysChem **20**, 1272 (2019).
[14]P. I. Kingsbury, Jr., W. D. Ohlsen, and O. W. Johnson, Phys. Rev. **175**, 1099 (1968).
[15]A. T. Brant, N. C. Giles, and L. E. Halliburton, J. Appl. Phys. **113**, 053712 (2013).
[16]V. N. Bogomolov and D. N. Mirlin, ZhETF Pis'ma **5**, 293 (1967).
[17]P. F. Chester, J. Appl. Phys. **32**, 866 (1961).
[18]C. N. Duckworth, A. W. Brinkman, and J. Woods, Phys. Status Solidi A **75**, K99 (1983).
[19]S. Yang and L. E. Halliburton, Phys. Rev. B **81**, 035204 (2010).
[20]S. Yang, L. E. Halliburton, A. Manivannan, P. H. Bunton, D. B. Baker, M. Klemm, S. Horn, and A. Fujishima, Appl. Phys. Lett. **94**, 162114 (2009).
[21]A. T. Brant, E. M. Golden, N. C. Giles, S. Yang, M. A. R. Sarker, S. Watauchi, M. Nagao, I. Tanaka, D. A. Tryk, A. Manivannan, and L. E. Halliburton, Phys. Rev. B **89**, 115206 (2014).
[22]P. Deák, B. Aradi, and T. Frauenheim, Phys. Rev. B **86**, 195206 (2012).
[23]A. Janotti, C. Franchini, J. B. Varley, G. Kresse, and C. G. Van de Walle, Phys. Status Solidi RRL **7**, 199 (2013).
[24]J. W. DeFord and O. W. Johnson, J. Appl. Phys. **54**, 889 (1983).
[25]P. F. Chester, J. Appl. Phys. **32**, 2233 (1961).
[26]P. I. Kingsbury, Jr., W. D. Ohlsen, and O. W. Johnson, Phys. Rev. **175**, 1091 (1968).
[27]R. R. Hasiguti and E. Yagi, Phys. Rev. B **49**, 7251 (1994).
[28]E. Yagi, R. R. Hasiguti, and M. Aono, Phys. Rev. B **54**, 7945 (1996).
[29]A. T. Brant, S. Yang, N. C. Giles, and L. E. Halliburton, J. Appl. Phys. **110**, 053714 (2011).
[30]W. D. Ohlsen and O. W. Johnson, J. Appl. Phys. **44**, 1927 (1973).
[31]M. Stavola, F. Bekisli, W. Yin, K. Smithe, W. B. Fowler, and L. A. Boatner, J. Appl. Phys. **115**, 012001 (2014).
[32]E. V. Lavrov, Phys. Rev. B **93**, 045204 (2016).
[33]H. Y. Fan, "Effects of free carriers on the optical properties," in *Chapter 9 in Optical Properties of III-V Compounds, Vol. 3 in the Series Semiconductors and Semimetals*, edited by R. K. Willardson and A. C. Beer (Academic Press, 1967).
[34]L. E. Halliburton, "Electron traps in rutile TiO_2 crystals: Intrinsic small polarons, impurities, and oxygen vacancies," MRS Proc. **1731**, 1–12 (2015).
[35]B. H. Soffer, J. Chem. Phys. **35**, 940 (1961).
[36]R. G. Breckenridge and W. R. Hosler, Phys. Rev. **91**, 793 (1953).
[37]V. M. Khomenko, K. Langer, H. Rager, and A. Fett, Phys. Chem. Miner. **25**, 338 (1998).
[38]O. F. Schirmer, M. Imlau, C. Merschjann, and B. Schoke, J. Phys. Condens. Matter **21**, 123201 (2009).
[39]C. N. Berglund and H. J. Braun, Phys. Rev. **164**, 790 (1967).
[40]M. Schrader, D. Mienert, T.-S. Oh, H.-I. Yoo, and K. D. Becker, Solid State Sci. **10**, 768 (2008).
[41]M. F. Saenger, T. Höing, B. W. Robertson, R. B. Billa, T. Hofman, E. Schubert, and M. Schubert, Phys. Rev. B **78**, 245205 (2008).
[42]V. N. Bogomolov and D. N. Mirlin, Phys. Status Solidi B **27**, 443 (1968).
[43]R. C. Vilão, R. B. L. Vieira, H. V. Alberto, J. M. Gil, A. Weidinger, R. L. Lichti, B. B. Baker, P. W. Mengyan, and J. S. Lord, Phys. Rev. B **92**, 081202 (R) (2015).
[44]K. Shimomura, R. Kadono, A. Koda, K. Nishiyama, and M. Mihara, Phys. Rev. B **92**, 075203 (2015).
[45]A. R. Elmaslmane, M. B. Watkins, and K. P. McKenna, J. Chem. Theory Comput. **14**, 3740 (2018).
[46]M. O. Atambo, D. Varsano, A. Ferretti, S. S. Ataei, M. J. Caldas, E. Molinari, and A. Selloni, Phys. Rev. Mater. **3**, 045401 (2019).
[47]B. J. Morgan, D. O. Scanlon, and G. W. Watson, J. Mater. Chem. **19**, 5175 (2009).
[48]M. Setvin, C. Franchini, X. Hao, M. Schmid, A. Janotti, M. Kaltak, C. G. Van de Walle, G. Kresse, and U. Diebold, Phys. Rev. Lett. **113**, 086402 (2014).
[49]D. A. Panayotov, S. P. Burrows, and J. R. Morris, J. Phys. Chem. C **116**, 4535 (2012).
[50]M. D. McCluskey, M. C. Tarun, and S. T. Teklemichael, J. Mater. Res. **27**, 2190 (2012).
[51]M. Stavola and W. B. Fowler, J. Appl. Phys. **123**, 161561 (2018).
[52]O. W. Johnson, W. D. Ohlsen, and P. I. Kingsbury, Jr., Phys. Rev. **175**, 1102 (1968).
[53]A. Hupfer, L. Vines, E. V. Monakhov, B. G. Svensson, and F. Herklotz, Phys. Rev. B **96**, 085203 (2017).
[54]J. B. Bates and R. A. Perkins, Phys. Rev. B **16**, 3713 (1977).
[55]F. Herklotz, E. V. Lavrov, and J. Weber, Phys. Rev. B **83**, 235202 (2011).
[56]E. V. Lavrov, T. Mchedlidze, and F. Herklotz, J. Appl. Phys. **120**, 055703 (2016).
[57]F. Bekisli, W. Beall Fowler, and M. Stavola, Phys. Rev. B **86**, 155208 (2012).
[58]M. D. McCluskey, S. J. Jokela, K. K. Zhuravlev, P. J. Simpson, and K. G. Lynn, Appl. Phys. Lett. **81**, 3807 (2002).
[59]G. A. Shi, M. Stavola, S. J. Pearton, M. Thieme, E. V. Lavrov, and J. Weber, Phys. Rev. B **72**, 195211 (2005).
[60]E. V. Lavrov, F. Herklotz, and J. Weber, Phys. Rev. B **79**, 165210 (2009).
[61]W. Yin, K. Smithe, P. Weiser, M. Stavola, W. B. Fowler, L. Boatner, S. J. Pearton, D. C. Hays, and S. G. Koch, Phys. Rev. B **91**, 075208 (2015).
[62]W. M. Hlaing Oo, S. Tabatabaei, M. D. McCluskey, J. B. Varley, A. Janotti, and C. G. Van de Walle, Phys. Rev. B **82**, 193201 (2010).
[63]F. Bekisli, M. Stavola, W. B. Fowler, L. Boatner, E. Spahr, and G. Lüpke, Phys. Rev. B **84**, 035213 (2011).
[64]Y. Qin, M. Stavola, W. B. Fowler, P. Weiser, and S. J. Pearton, ECS J. Solid State Sci. Technol. **8**, Q3103 (2019).
[65]A. Nitta, M. Takase, M. Takashima, N. Murakami, and B. Ohtani, Chem. Commun. **52**, 12096 (2016).
[66]A. Nitta, M. Takashima, M. Takase, and B. Ohtani, Catal. Today **321–322**, 2 (2019).
[67]M. Kato, H. Najima, and T. Ozawa, J. Electrochem. Soc. **166**, H468 (2019).
[68]L.-B. Mo, Y. Wang, Q. Xiang, Q. Li, W. Yao, J. Wang, K. Ibrahim, H. Wang, C. Wan, and J. Cao, Sci. Rep. **5**, 17634 (2015).
[69]T. S. Bjørheim, A. Kuwabara, and T. Norby, J. Phys. Chem. C **117**, 5919 (2013).
[70]W. H. Sio, C. Verdi, S. Poncé, and F. Giustino, Phys. Rev. Lett. **122**, 246403 (2019).
[71]W. H. Sio, C. Verdi, S. Poncé, and F. Giustino, Phys. Rev. B **99**, 235139 (2019).
[72]See https://www.mtixtl.com/tio2substrates.aspx for "Float-zone-grown rutile TiO_2 single crystals from MTI Corporation".
[73]See https://www.shinkosha.com/english/product/epi_substrate/epi_substrate_03/ for "Verneuil-grown rutile TiO_2 single crystals from Shinkosha Co., Ltd".
[74]J. Bonkerud, C. Zimmermann, P. M. Weiser, T. Aarholt, E. F. Verhoeven, L. Vines, E. V. Monakhov, and F. Herklotz, Mater. Res. Exp. **7**, 065903 (2020).
[75]C. Zimmermann, J. Bonkerud, F. Herklotz, T. N. Sky, A. Hupfer, E. Monakhov, B. G. Svensson, and L. Vines, J. Appl. Phys. **123**, 161572 (2018).
[76]P. Blood and J. W. Orton, *The Electrical Characterization of Semiconductors: Majority Carriers and Electron States* (Academic Press, 1992).
[77]L. J. Van der Pauw, Philips Tech. Rev. **20**, 220 (1958).
[78]J. D. Weiss, R. J. Kaplar, and K. E. Kambour, Solid State Electron. **52**, 91 (2008).
[79]M. Fox, *Optical Properties of Solids*, 2nd ed. (Oxford University Press Inc., 2010).
[80]S. Schöche, T. Hofmann, R. Korlacki, T. E. Tiwald, and M. Schubert, J. Appl. Phys. **113**, 164102 (2013).

[81]O. W. Johnson, J. DeFord, and J. W. Shaner, J. Appl. Phys. **44**, 3008 (1973).
[82]We attempted room temperature Hall effect measurements on two H-doped samples (FG-annealed at 600 °C for 50 and 75 min, respectively), which yielded mobilities of 0.2–0.3 $cm^2 V^{-1} s^{-1}$ for both samples. However, the uncertainties in these values are of the same order of magnitude (±0.2 $cm^2 V^{-1} s^{-1}$). Given that our Hall setup is not rated for mobilities less than 1 $cm^2 V^{-1} s^{-1}$, the apparent agreement between the Hall mobility and that determined from optical absorption measurements is likely coincidental.
[83]A. A. Kopylov and A. N. Pikhtin, Sov. Phys. Solid State **16**, 1200 (1975).
[84]X. Han, N. Amrane, Z. Zhang, and M. Benkraouda, J. Phys. Chem. C **123**, 2037 (2019).